High-energy lithium-ion hybrid supercapacitors composed of hierarchical urchin-like WO₃/C anodes and MOF-derived polyhedral hollow carbon cathodes†

Juan Xu,[a] Yuanyuan Li,[a] Lei Wang,[a] Qifa Cai,[a] Qingwei Li,[a,c] Biao Gao,[b] Xuming Zhang,[b,c] Kaifu Huo*[a] and Paul K. Chu[c]

A lithium-ion hybrid supercapacitor (Li-HSC) comprising a Li-ion battery type anode and an electrochemical double layer capacitance (EDLC) type cathode has attracted much interest because it accomplishes a large energy density without compromising the power density. In this work, hierarchical carbon coated WO_3 (WO_3/C) with a unique mesoporous structure and metal–organic framework derived nitrogen-doped carbon hollow polyhedra (MOF-NC) are prepared and adopted as the anode and the cathode for Li-HSCs. The hierarchical mesoporous WO_3/C microspheres assembled by radially oriented WO_3/C nanorods along the (001) plane enable effective Li^+ insertion, thus exhibit high capacity, excellent rate performance and a long cycling life due to their high Li^+ conductivity, electronic conductivity and structural robustness. The WO_3/C structure shows a reversible specific capacity of 508 mA h g^{-1} at a 0.1 C rate (1 C = 696 mA h g^{-1}) after 160 discharging–charging cycles with excellent rate capability. The MOF-NC achieved the specific capacity of 269.9 F g^{-1} at a current density of 0.2 A g^{-1}. At a high current density of 6 A g^{-1}, 92.4% of the initial capacity could be retained after 2000 discharging–charging cycles, suggesting excellent cycle stability. The Li-HSC comprising a WO_3/C anode and a MOF-NC cathode boasts a large energy density of 159.97 W h kg^{-1} at a power density of 173.6 W kg^{-1} and 88.3% of the capacity is retained at a current density of 5 A g^{-1} after 3000 charging-discharging cycles, which are better than those previously reported for Li-HSCs. The high energy and power densities of the Li-HSCs of WO_3/C//MOF-NC render large potential in energy storage.

Introduction

Owing to the depletion of fossil fuels and ever-worsening environmental pollution, there is increasing demand for sustainable and renewable energy sources as well as highly efficient energy storage devices.[1] Li-ion batteries (LIBs) and supercapacitors (SCs) constitute the two main types of electrochemical energy storage devices in portable electronics,

electric vehicles (EVs), and hybrid electric vehicles (HEVs).[2–5] LIBs could deliver a large energy density but suffer from low power density and cycling performance due to sluggish solid-state Li-ion diffusion through the active materials and the accompanying volumetric strain.[6] Different from LIBs, electric doubled-layer capacitors (EDLCs) store charges by fast physical adsorption/desorption of solvated ions at the electrolyte–electrode interfaces. As a result, EDLCs exhibit large power densities, fast charging–discharging rates, and long-term recyclability, but their energy densities (generally below 10 kW kg^{-1}) are relatively low.[7] Recently, Li-ion hybrid supercapacitors (Li-HSCs) have been proposed as potential energy storage devices because they combine the large energy and high power densities offered by LIBs and SCs.[2,3,8] In Li-HSCs, charges are stored by reversible anion adsorption/desorption at the cathode surface and Faradaic Li^+ insertion/desertion reactions at the anode. The battery-like electrode provides a high specific capacity while the capacitive electrode supplies a large power density. Additionally, the use of organic

*a*Wuhan National Laboratory for Optoelectronics (WNLO), School of Optical and Electronic Information, Huazhong University of Science and Technology, Wuhan 430074, China. E-mail: kfhuo@hust.edu.cn
*b*The State Key Laboratory of Refractories and Metallurgy, Wuhan University of Science and Technology, Wuhan 430081, China
*c*Department of Physics and Materials Science, City University of Hong Kong, Tat Chee Avenue, Kowloon, Hong Kong, China
†Electronic supplementary information (ESI) available: SEM of pristine WO₃, high-resolution XPS spectra of C 1s and pore size distribution of urchin-like WO₃/C microspheres, the CV curves of pristine WO₃//Li half-cells, and the high resolution XPS spectra of MOF-NC. See DOI: 10.1039/c6nr05480c

electrolytes provides a large voltage window and so Li-HSCs are potentially high-performance electrochemical energy storage devices.[9]

The energy storage properties of Li-HSCs depend largely on the electrode materials. Amatucci *et al.* prepared a Li-HSC using nanostructured $Li_4Ti_5O_{12}$ (LTO) as the negative material and activated carbon (AC) as the positive material showing an energy density of 20 W h kg^{-1} that was larger than those of conventional SCs.[2,8] In addition, various Li-HSCs composed of LTO anodes and carbon cathodes such as graphene, nanotubes, and activated carbon (AC) have been prepared to have promising energy storage properties.[7,10,11] However, the energy density of Li-HSCs comprising LTO anodes is limited by the relatively high Li^+ insertion/desertion potential (>1.5 V) and low specific capacity (~175 mA h g^{-1}) of LTO.[7,9,11] Moreover, the low Li^+ diffusion coefficient and poor electron conductivity of LTO hamper the rate performance and power density of Li-HSCs.[12,13]

Transition metal oxides (TMOs) such as Nb_2O_5[14–16] and MnO_2[17,18] are promising anode materials in Li-HSCs due to their large theoretical specific capacity and relatively low voltage plateau. As typical intercalated host materials for alkalis, hexagonal WO_3 (h-WO_3) shows great promise in electrochemical energy storage due to its high theoretical capacity (696 mA h g^{-1}) and the well-known tunnel structure facilitating diffusion and transport of Li^+.[19–21] For example, Duan *et al.*[19] disclosed that h-WO_3 mesocrystals with the biconical morphology could deliver a high capacity of 400 mA h g^{-1} after 50 charging/discharging cycles and Lee *et al.*[20] reported a flexible anode film electrode composed of reduced WO_3 and carbon nanofibers (WO_x–CNF) boasting a high reversible capacity of 481 mA h g^{-1}. Compared to h-WO_3 mesocrystals or nanofibers, mesoporous microspheres assembled with three-dimensional (3D) h-WO_3 nanorods could buffer the physical strain and stress during charging and discharging, shorten the diffusion lengths of electrons and lithium ions, and improve the electrochemical kinetics and cyclability of the electrode materials.[22] Furthermore, mesoporous microspheres assembled by radially oriented WO_3 nanorods have a larger volumetric energy density due to the larger tap density. To improve the rate capability, the semiconducting WO_3 is generally mixed with a conducting matrix or directly grown on a conducting matrix such as carbon.[23] However, simple mechanical mixing with conducting agents such as carbon materials cannot guarantee homogeneous mixing thus limiting the full utilization of the charge storage capability of WO_3. Therefore, it is desirable to design carbon-coated WO_3 (WO_3/C) nanorod assembled hierarchical mesoporous microspheres to maximize the potential of WO_3 for Li-HSCs by offering high electrical conductivity, structural stability, as well as fast ion diffusion and electron transport. However, such 3D hierarchical mesoporous WO_3/C electrode materials as well as Li-HSCs have not been reported to date.

Activated carbon (AC) is the most widely used cathode materials in Li-HSCs on account of the large specific surface area and chemical stability. However, the specific capacitance of AC is relatively low, especially at large charging–discharging currents thereby limiting the energy density of Li-HSCs at large power densities. Recently, large-surface-area porous carbon materials derived from metal–organic frameworks (MOFs) have been demonstrated as electrode materials in supercapacitors.[24] The MOF-derived carbon materials have many functionalities and tunable porosities thus providing abundant active sites for energy storage. Hence, the performance of Li-HSCs may be improved by adopting cathodes of MOF-derived carbon materials instead of AC.

Herein, we report high-energy Li-HSCs composed of urchin-like WO_3/C microspheres assembled by WO_3/C nanorods as the anode and MOF-derived nitrogen-doped carbon (MOF-NC) hollow polyhedra as the cathode. The hierarchical urchin-like WO_3/C microspheres have a porous 3D architecture consisting of assembled WO_3/C nanorods, which provide a large accessible surface to the electrolyte, shorten the Li^+ and e^- diffusion lengths, and enhance the conductivity. The hierarchical urchin-like WO_3/C microspheres deliver a high specific capacity of 508 mA h g^{-1} at a current density of 0.1 C (1 C = 696 mA h g^{-1}) after 160 discharging–charging cycles. The MOF-NC achieved the specific capacity of 269.9 F g^{-1} at a current density of 0.2 A g^{-1}. At a high current density of 6 A g^{-1}, 92.4% of the initial capacity could be retained after 2000 discharging–charging cycles, suggesting excellent cycle stability. The Li-HSC constructed by the mesoporous WO_3/C microspheres anode and the MOF-NC cathode deliver a large energy density of 160.0 W h kg^{-1} at a power density of 173.6 W kg^{-1} and 88.3% of the capacity is retained at the current density of 5 A g^{-1} after 3000 charging–discharging cycles. The performance is better than previously-reported Li-HSCs.[23–25]

Experimental details

Synthesis of WO_3 microspheres comprising urchin-like WO_3 nanorods

All the reactants and solvents were of analytical grade and used without further purification. The WO_3 microspheres consisting of urchin-like WO_3 nanorods were produced hydrothermally. In a typical process, 0.72 g of K_2WO_4 was dispersed in 20 ml of deionized water (DI) to form a clear solution and HCl (6 M) was added dropwise under magnetic stirring until the pH was close to 2. Subsequently, 6 ml of H_2O_2 was added slowly to the suspension until the solution was transparent. It was then transferred to an autoclave and heated to 160 °C for 6 h. The hydrothermal product was collected by centrifugation and rinsed several times with DI water and ethanol.

Synthesis of urchin-like microspheres comprising assembled WO_3/C nanorods

The as-synthesized urchin-like WO_3 microspheres were dispersed in 20 mL of DI water and sonicated for 30 min followed by addition of 0.65 g glucose to the solution. The solution was transferred to an autoclave in an oven and heated to 160 °C for 10 h. The hydrothermal products were further thermally

treated at 600 °C for 3 h in a tube furnace under Ar to produce the microspheres consisting of urchin-like WO_3/C nanorods.

Synthesis of Zn-MOF and MOF-NC

The Zn-MOF was prepared using the previously reported method.[22] In a typical synthesis, 100 mg of zinc acetate ($Zn(CH_3COOH)_2 \cdot 6H_2O$) were added to 50 ml of methanol to form a solution which was then added to 50 ml of a solution containing 2-methylimidazole (105.0 mg) and polyvinylpyrrolidone (K-30, 0.3 g) using a syringe under sonication. After stirring for 30 min, the reaction was aged at room temperature for 9 h. The resulting white precipitate was centrifuged, washed several times with methanol, and vacuum-dried at 60 °C. The samples were further carbonized at 800 °C and the residual Zn was etched with HCl to produce the MOF-NC.

Materials characterization

The morphology, structure, and composition of the samples were characterized by X-ray diffraction (XRD, X'Pert PRO, PANanalytical B.V., Netherlands) with radiation from a Cu target (Kα, λ = 0.15406 nm), field-emission scanning electron microscopy (FE-SEM, FEI Nova NanoSEM 450) equipped with an X-ray energy dispersive spectrometer (EDS), transmission electron microscopy (TEM, FEI Tecnai G20), Raman scattering (InVo-RENISHAW), Fourier transform infrared spectroscopy (FT-IR, Bruker Vertex 80 V), and X-ray photoelectron spectroscopy (XPS, Kratos AXIS Ultra DLD-600 W). The thermo gravimetric-differential analysis (TG-DSC) was performed on the Perkin Elmer Diamond TG-DTA at a temperature ramping rate of 5 °C min^{-1} under air.

Electrochemical measurements

The electrochemical performance of the urchin-like WO_3/C microspheres and MOF-NC was assessed using CR-2025 coin-type cells with a lithium foil serving as the counter electrode. The working electrode was prepared by mixing 80 wt% of the active materials, 10 wt% of acetylene black (Super-P), and 10 wt% of poly(vinyl difluoride) (PVDF) in N-methyl-2-pyrrolidone (NMP). The mixture was coated onto a copper foil/aluminium foil by a doctor blade method. The electrodes were dried at 80 °C in a vacuum oven overnight to remove the solvent and then roll-pressed. A Celgard 2400 film was used as the separator. The electrolyte consisted of 1 M $LiPF_6$ in ethylene (EC)/dimethyl carbonate (DMC) (1 : 1 w/w).

The Li-HSCs were assembled into coin-like cells with pre-lithiated WO_3/C as the anodes and MOF-NC as the cathodes. The mass ratio of the cathode/anode was 7.6 : 1 based on charge balance. The WO_3/C anode was obtained by lithiation of WO_3/C after 2 cycles at a low current density of 0.1 C (1 C = 696 mA h g^{-1}) with a Li foil as the counter electrode. Cyclic voltammetry (CV) was performed at scan rates from 0.05 to 0.5 V s^{-1} and galvanostatic charging–discharging (GCD) was conducted at current densities of 0.5, 1, 2, 3 and 5 A g^{-1}. Electrochemical impedance spectroscopy (EIS) was performed at the open circuit potential with a 5 mV amplitude at frequencies between 10 mHz and 100 kHz on an Autolab electrochemical workstation.

Results and discussion

Characterization of hierarchical WO_3/C microspheres

The synthesis process of urchin-like WO_3/C microspheres is illustrated in Scheme 1. The urchin-like WO_3 microspheres were prepared by a hydrothermal treatment of potassium tungstate ($K_2WO_4 \cdot 2H_2O$) and then coated with carbon by a glucose hydrothermal treatment followed by further thermal treatment at 600 °C under Ar (Scheme 1). The hierarchical urchin-like WO_3 microspheres are formed by assembling many radical 1D nanorods. The WO_3 NR grow along the (001) plane with hexagonal close-packed WO_6 octahedral channels which facilitate Li$^+$ transport through the crystal. The growth of urchin-like WO_3 microspheres is generally considered as the oriented aggregation mechanism.[26–28]

Fig. S1a (ESI†) depicts the low-magnification SEM image of the hydrothermal product showing urchin-like hierarchical microspherical particles with a size of 2–4 μm. The urchin-like microspheres are assembled by radially oriented nanorods. The corresponding XRD pattern is shown in Fig. 1a. The diffraction peaks originate from h-WO_3 (JCPDS Card no. 85-2460) indicating that the products consist of urchin-like hierarchical h-WO_3 microspheres. After coating with carbon, the SEM (Fig. 1b) and TEM images (Fig. 1c) reveal that the h-WO_3/C inherits the morphology of the urchin-like hierarchical structure in which the radial nanorods are assembled into urchin-like microspheres. The radial nanorods have a diameter of 50–100 nm and facet morphology (Fig. S1b, ESI†). The XRD patterns of the urchin-like hierarchical h-WO_3/C is the same as those of h-WO_3 and no carbon peaks can be detected from h-WO_3/C possibly due to the disordered nature of the carbon coating. The high-resolution TEM image (Fig. 1d) of a typical h-WO_3/C nanorod reveals the core–shell morphology. The inner WO_3 nanorod has a single-crystal structure with periodic fringes of 0.38 nm corresponding to the (002) plane of h-WO_3. The outer carbon shell is amorphous with a thickness of 8–10 nm. The energy dispersive X-ray spectra (EDS) and elemental mappings of a typical urchin-like WO_3/C microsphere are shown in Fig. 1e. The blue, green, and red colours
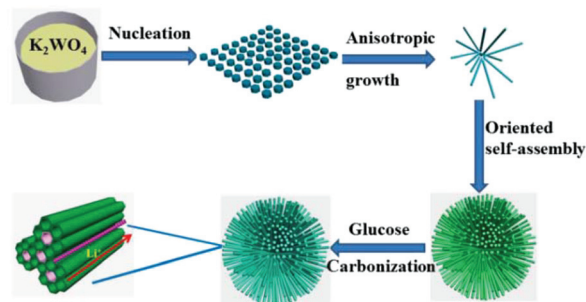
Scheme 1 Schematic illustration of the synthesis process of WO_3/C.

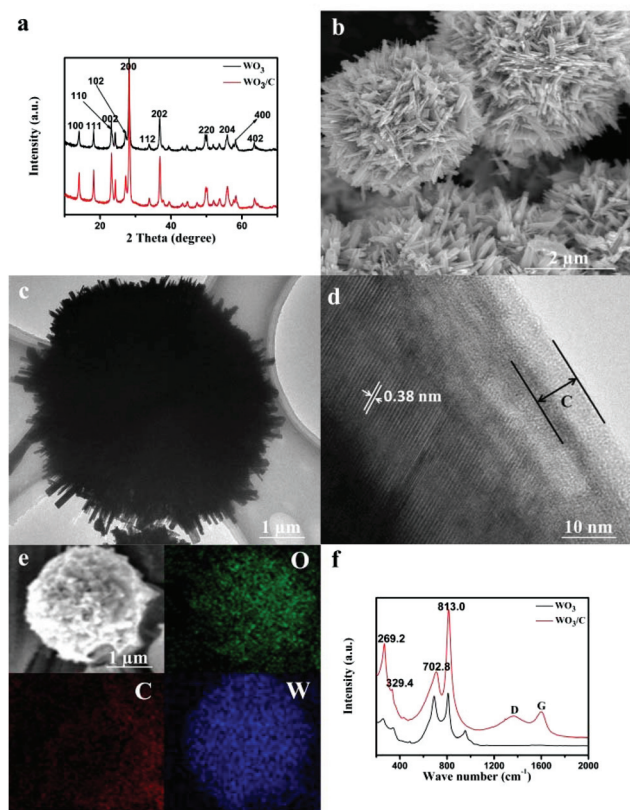Fig. 1 Characterization of the urchin-like WO₃/C microspheres: (a) XRD pattern; (b and c) SEM and TEM images of the urchin-like WO₃/C microspheres; (d) high-magnification TEM of a typical WO₃/C nanorod revealing single-crystal WO₃ coated with amorphous carbon; (e) elemental maps of a typical urchin-like WO₃/C microsphere. The blue, green and red colors represent W, O and C, respectively; (f) Raman spectra of the urchin-like WO₃/C microspheres.

represent W, O and C, respectively. The EDS mapping further reveals the uniform distribution of W, O, and C. The Raman spectra of the WO₃/C and WO₃ are shown in Fig. 1f. The four peaks located at 269.2, 329.4, 702.8, and 813.0 cm^{-1} can be attributed to the δ(O–W–O) bending modes and ν(O–W–O) stretching modes, respectively.[29] The peak at 952 cm^{-1} can be assigned to the stretching mode of the terminal W=O double bonds on the boundaries of the nanocrystals.[30] After deposition of the carbon coating, the peak at 952 cm^{-1} disappears and the two broad peaks at 1350 and 1580 cm^{-1} corresponding to the D band and the G band of the carbon shell can be identified from the WO₃/C. The G band is attributed to the vibration of sp^2-bonded carbon atoms in a 2D hexagonal lattice, whereas the D band is related to defects and disordered structures in the carbon.[31,32] The Raman results further corroborate the carbon coating on the urchin-like WO₃/C microspheres.

The X-ray photoelectron spectroscopy (XPS) results acquired from the urchin-like WO₃/C microspheres are shown in Fig. 2a and b. The survey spectrum reveals the presence of C, O, and W. The two fine XPS peaks of W (Fig. 2b) at 36.03 and 38.48 eV correspond to $4f_{7/2}$ and $4f_{5/2}$ of W^{6+},[33,34] in agreement with the
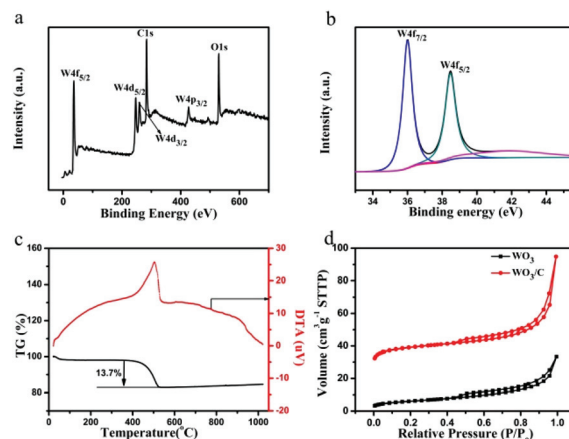

Fig. 2 (a) Survey XPS and (b) high-resolution W spectrum of the mesoporous WO₃/C microspheres; (c) TGA and DSC profiles; (d) N₂ adsorption–desorption isotherms of the 3D porous WO₃/C hybrid.

XRD pattern of WO₃ (Fig. 1a). No XPS signal related to W–C bonding is observed from the fine spectra of W and C (Fig. S2, ESI†) further supporting the formation of C-coated WO₃. The C content in WO₃/C is measured to be 13.7 wt% according to the TG curve in Fig. 2c. The nitrogen adsorption–desorption isotherms of the urchin-like and WO₃ microspheres disclose the typical mesoporous characteristics (Fig. 2d and S3, ESI†) and the Brunauer–Emmett–Teller (BET) surface areas are about 127.3 $m^2\ g^{-1}$ (WO₃/C) and 21.35 $m^2\ g^{-1}$ (WO₃), respectively. The larger surface area of WO₃/C compared to WO₃ can be ascribed to the mesoporous carbon coating since WO₃/C and WO₃ have the same structure and morphology. The urchin-like WO₃/C microspheres comprising radially assembled WO₃/C nanorods have a mesoporous 3D architecture thus providing a large accessible surface area to the electrolyte, structural stability, and short Li^+ and e^- diffusion lengths. Moreover, the homogeneous carbon coating on the WO₃ nanorods improves the conductivity and the radial WO₃ nanorods along the (001) plane enable effective Li^+ insertion and extraction within the hexagonal close-packed WO_6 octahedral channels giving rise to excellent cycling stability during charging and discharging. The synergism rendered by the unique morphology, structure, and composition of the urchin-like WO₃/C microspheres leads to excellent electrochemical performance in energy storage.

Electrochemical characterization of hierarchical urchin-like WO₃/C microspheres

To evaluate the electrochemical performance of the WO₃/C microspheres, half-cells are assembled using 2025-type coin cells with a lithium foil as the counter electrode and 1 M LiPF₆ in a mixture of ethylene carbonate (EC) and dimethyl carbonate (DMC) (v/v = 1 : 1) as the electrolyte. Fig. 3a shows the charging–discharging curves of the WO₃/C hierarchical microspheres at a current density of 0.1 C. In a previous study, the WO₃ electrode materials generally exhibited fast capacity degradation during the initial several cycles.[28,35,36] For
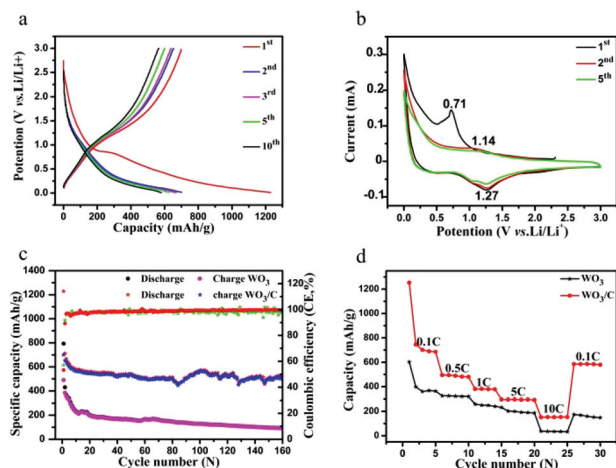
Fig. 3 Electrochemical performance of the WO$_3$/C hierarchical microspheres (the specific capacity is calculated based on the mass of the active material): (a) galvanostatic charging–discharging profiles of WO$_3$/C at a rate of 0.1 C (1 C = 696 mA h g^{-1}); (b) CV curves at a scanning rate of 0.1 mV s^{-1} in the voltage range of 0–3.0 V vs. Li/Li$^+$; (c) cycling performance of the hierarchical WO$_3$/C and WO$_3$ microspheres at 0.1 C; (d) rate capability at various current densities from 0.1 to 10 C.

comparison, our WO$_3$/C hierarchical microspheres show a slow decrease during the first 10 cycles revealing improved reversible cycling ability. The initial discharging (lithiation) and charging (delithiation) capacities are 1229.5 and 699.8 mA h g^{-1}, respectively, based on the mass loading of the active materials, implying 56% initial coulombic efficiency. The high irreversible capacity loss in the first cycle can be ascribed to the irreversible formation of the solid electrolyte interface (SEI) film. Fig. 3b depicts the cyclic voltammetry (CV) curves of the WO$_3$/C electrode in the first five discharging–charging cycles at a scanning rate of 0.1 mV s^{-1}. In the CV curves, a strong peak at 0.71 V is observed during the first cycle but it disappears from subsequent cycles. It is related to the initial reduction of WO$_3$ and formation of the SEI layer on WO$_3$/C. The two peaks at 1.14 V (anodic curve) and 1.27 V (cathodic curve) are associated with the reversible phase transition of WO$_3$/C in the lithiation/delithiation process. The anodic peaks at 1.14 V correspond to the reaction of WO$_3$ + 6Li$^+$ + 6e$^-$ → W + 3Li$_2$O.[28] Meanwhile, the cathodic peak at 1.27 V is attributed to oxidation of W to WO$_3$ and decomposition of Li$_2$O. The CV curves of the urchin-like WO$_3$ exhibited a reduced area during the first 5 cycles (Fig. S4, ESI†), however, the CV profiles of the urchin-like WO$_3$/C microspheres overlap after the first cycle, indicating good reversibility and excellent stability during lithiation/delithiation. The small voltage separation between the anodic and cathodic peak potentials in CVs further indicates that Li$^+$ insertion/extraction into/from the urchin-like WO$_3$/C microspheres is highly reversible. Fig. 3c presents the cycling performance of the WO$_3$ and WO$_3$/C hybrids as well as the corresponding Coulombic efficiency at a rate of 0.1 C. The capacities of both electrodes diminish slightly in the first few cycles and become stable. After the first 10 cycles, the hierarchical WO$_3$/C microspheres show a very stable discharging

capacity of 508 mA h g^{-1} even after 160 cycles, while the specific capacity of WO$_3$ decreases gradually to 91.8 mA h g^{-1} after 160 cycles. The specific capacity of the hierarchical WO$_3$/C microspheres is higher than that reported for WO$_3$ anode materials such as WO$_3$ nanowires, nanoparticles and mesoporous WO$_3$.[20–22] The improved cycling stability and large specific capacity can be attributed to the synergistic effects of the unique structure of the urchin-like WO$_3$ nanorods and carbon coating in combination with high electron mobility thereby resulting in full utilization of the charge storage capability of WO$_3$. Fig. 3d displays the rate performance of the urchin-like WO$_3$ and WO$_3$/C microspheres at various current densities ranging from 0.1 to 10 C in the voltage range of 0–3 V (vs. Li/Li$^+$). The discharging capacities of WO$_3$/C are 685.3, 480.3, 378.4, 292.6, and 152.7 mA h g^{-1} compared to 363.2, 319.8, 240.9, 186.9, and 32.1 mA h g^{-1} for the pristine WO$_3$ at current densities of 0.1, 0.5, 1, 5, and 10 C, respectively, suggesting that the WO$_3$/C electrode has better rate capability.

Synthesis and characterization of MOF-NC

The nitrogen-doped porous carbon materials are fabricated through carbonizing Zn-MOF.[22,37] The SEM image (Fig. 4a) discloses a polyhedron-like morphology with a size of 400 nm and the hollow polyhedral morphology is corroborated by the high-resolution TEM image (Fig. 4b). Nitrogen adsorption/desorption experiments are performed to measure the surface area of the MOF-NC. The nitrogen adsorption/desorption curve (Fig. 4c) clearly demonstrates the microporous and mesoporous characteristics and the measured BET surface is 1473.8 m^2 g^{-1}, in which the specific surface areas of micropores and mesopores are about 496.3 and 974.6 m^2 g^{-1}, respectively. The pores of MOF-NC are formed because of self-activation of Zn metal and subsequent carbonization.[24] Fig. 4d shows the Raman spectra of the MOF-NC. The G band corresponds to the graphitic layers and the D band is characteristic of disordered carbon or defective graphitic structures. The
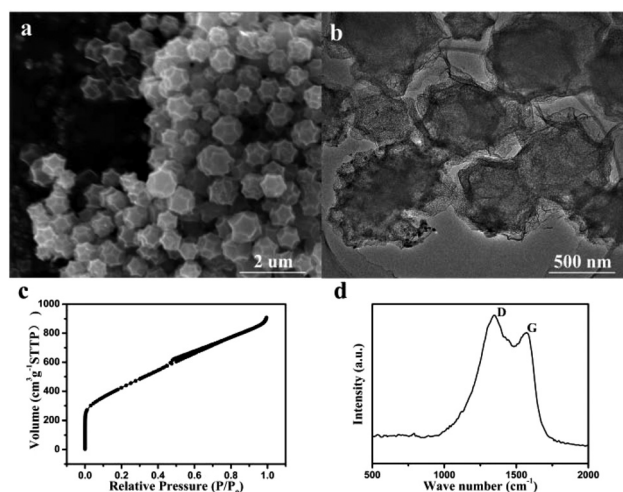

Fig. 4 (a) SEM images of MOF-NC; (b) TEM image; (c) nitrogen adsorption–desorption isotherms; (d) Raman scattering spectra.

high I_D/I_G ratio suggests good graphitization. The presence of N in the MOF-NC results in an asymmetric tailing of the D band extending out to about 1000 cm^{-1} as well as broadening and overlapping of D and G bands. The XPS (Fig. S5, ESI†) shows that N 1s spectra can be convoluted into three peaks, pyridinic-N (N-6, 398.6 eV), pyrrolic-N (N-5, 400.4 eV) and graphic-N (401.8 eV), further suggesting the formation of MOF-NC.

Electrochemical characterization of MOF-NC

The electrochemical performance of MOF-NC is evaluated by using half-cells. Fig. 5a shows the CV curves in the voltage range of 3–4.1 V (vs. Li/Li$^+$) at scanning rates between 20 and 200 mV s^{-1}. The CV curves exhibit a quasi-rectangular shape and it can be concluded that the charge storage mechanism is based on the electric double-layer. Fig. 5b shows the typical GCD curves for MOF-NC cycling between 3 and 4.1 V vs. Li/Li$^+$. A linear increase with time (i.e. potential) is noted further indicating perfect electric double layer formation across the electrode–electrolyte interface. The specific capacity of 269.9 F g^{-1} can be achieved at a current density of 0.2 A g^{-1}. The observed specific capacity can be converted into capacity by the following equation:

$$C\left(\mathrm{F\,g^{-1}}\right) = \frac{i(\mathrm{A}) \times t(\mathrm{s})}{\mathrm{dV(V)} \times m(\mathrm{g})} = \mathrm{mA\,h\,g^{-1}} \times \frac{3600}{\mathrm{dV(mV)}} \quad (1)$$

where i is the applied current, t is the discharge time, m is the weight of the active material and dV is the potential window of the single electrode configuration.[31] The capacity calculated from the above equation is about 82.4 mA h g^{-1}, which is considerably larger than that of commercial AC because of the presence of high-density micropores and mesopores. No

obvious IR drop is observed from the GCD curves, demonstrating superior rate performance of MOF-NC electrodes. Fig. 5c shows the calculated specific capacitance of MOF-NC as a function of current densities. 63% capacitance is retained when the current density is increased 30 fold from 0.2 to 6 A g^{-1}, suggesting excellent rate performance. More importantly, 92.4% of the initial capacity is retained after 2000 cycles at a current density of 6 A g^{-1} (Fig. 5d). The excellent performance shows that MOF-NC is a promising cathode in high-energy-density Li-HSCs.

Li-HSCs based on the urchin-like WO₃/C microspheres and MOF-NC

The Li-HSC is assembled using the pre-lithiated-WO₃/C electrode as the anode and MOF-NC as the cathode as shown in Scheme 2. To maximize the energy and power densities of the Li-HSCs, the mass ratio of the active cathode and anode materials is optimized to achieve charge balance between the two electrodes. The stored charge (Q) in each electrode is determined by $Q = C \times \Delta E \times m$, where C is the specific capacitance, ΔE is the potential range in charging/discharging, and m is the mass of the single electrode.[38] The Li-HSCs are assembled with WO₃/C and MOF-NC as the anode and the cathode at a mass ratio of 1 : 7.6 and the electrolyte contains 1 M LiPF₆ in a mixture of ethylene carbonate (EC) and dimethyl carbonate (DMC) (v/v = 1 : 1).

Fig. 6a shows the CV curves at different scanning rates. The CV curves maintain a relatively quasi-rectangular shape and obvious peaks even at scanning rates up to 500 mV s^{-1}, suggesting fast electrolyte ion transport and redox pseudocapacitive behaviour. During the charging process, PF₆⁻ ions are absorbed by the porous structure of MOF-NC (positive electrode) and Li$^+$ ions from the electrolyte are intercalated into the WO₃/C microspheres (negative electrode). The discharging process is opposite to the charging process. The charge–discharge curves of the Li-HSCs (WO₃/C//MOF-NC) based on the
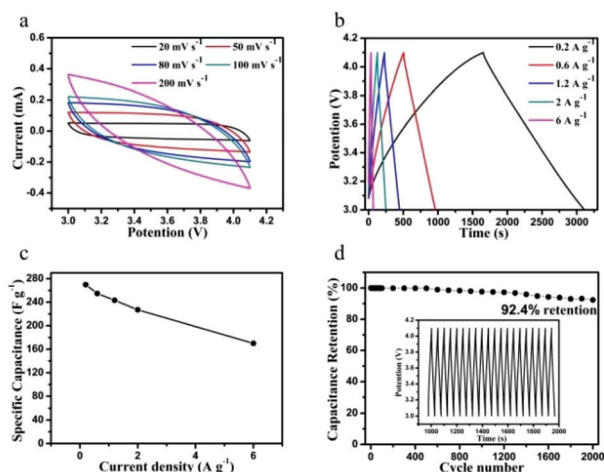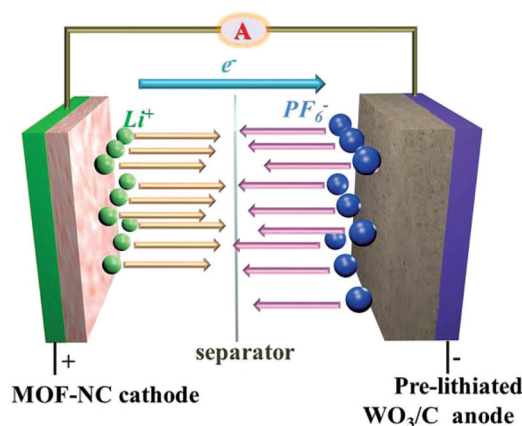

Fig. 5 Electrochemical performance of MOF-NC: (a) CV curves at various scanning rates from 20 to 200 mV s^{-1}. (b) Galvanostatic charging–discharging profiles at various current densities from 0.2 to 6 A g^{-1}. (c) Gravimetric capacitance as a function of current density. (d) Cycling performance during 2000 charging–discharging cycles at a current density of 6 A g^{-1} with the inset showing the galvanostatic charging/discharging curves of the last 20 cycles.

Scheme 2 Schematic diagram of the charging process of Li-HSCs using MOF-NC as the cathode and pre-lithiated-WO₃/C hierarchical microspheres as the anode.
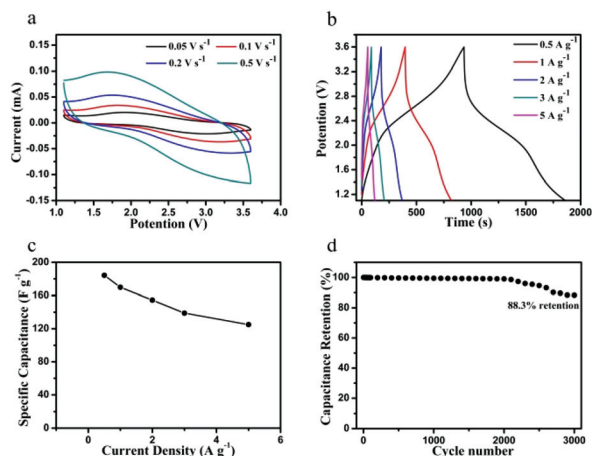
Fig. 6 Electrochemical performance of the Li-HSCs using WO_3/C as the anode and MOF-NC as the cathode: (a) CV curves at various scanning rates from 0.05 to 0.5 V s^{-1}. (b) Galvanostatic charging–discharging profiles at various current densities from 0.5 to 5 A g^{-1}. (c) Gravimetric capacitance as a function of current densities. (d) Cycling performance during 3000 charging–discharging cycles at a current density of 5 A g^{-1}.

WO_3/C anode and the MOF-NC cathode in Fig. 6b are not strictly linear especially at small current densities, demonstrating the unique characteristic of the combination of Li-ion batteries and supercapacitors. It is ascribed to the synergistic effects of two disparate energy-storage mechanisms: surface adsorption/desorption and redox reaction.[38] The discharging capacitance (C_{cell}) is calculated by the following relation $C_{cell} = (It/m\Delta V)$, where I is the applied current, t is the discharging time, and ΔV is the potential difference.[39] As expected, the Li-HSC shows 184.3 F g^{-1} at a current density of 0.5 A g^{-1} and it remains at 125.1 F g^{-1} at a large current density of 5 A g^{-1} (Fig. 6c), suggesting excellent rate capability. Moreover, the WO_3/C//MOF-NC Li-HSCs also show excellent cycle stability with 88.3% retention after 3000 cycles at a large current density of 5 A g^{-1} (Fig. 6d).
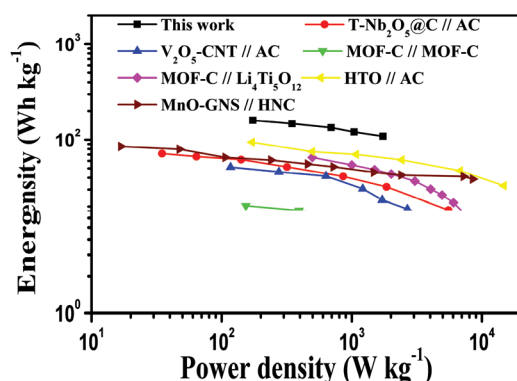
The Ragone plot (energy density *vs.* power density) of the WO_3/C//MOF-NC Li-HSCs is shown in Fig. 7. The energy density and power density are calculated based on the total mass of both electrodes. Both the energy density and power density of our Li-HSCs of WO_3/C//MOF-NC are much larger than those previously-reported Li-HSCs. At a power density of 173.6 W kg^{-1}, the Li-HSCs deliver a large energy density of 159.97 W h kg^{-1} and the energy density is maintained at 108.54 W h kg^{-1} by increasing the power density to 1736 W kg^{-1}. Furthermore, compared to other Li-HSCs such as T-Nb_2O_5/C//AC,[23] V_2O_5-CNT//AC,[24] MOF-C//MOF-C symmetric SC,[22] MOF-C//$Li_4Ti_5O_{12}$ hybrid SC,[22] HTO//AC HSC,[40] and MnO-GNS//HNC,[41] the WO_3/C//MOF-NC Li-HSCs exhibit a larger energy density with an improved power density as summarized in Fig. 7.

Conclusion

A Li-HSC comprising hierarchical urchin-like WO_3/C microspheres as the negative electrode and MOF-NC as the positive electrode is designed and produced. As a negative electrode, the mesoporous urchin-like WO_3/C assembled by radically oriented WO_3/C nanorods has both a high specific capacity of 508 mA h g^{-1} at 0.1 C after 160 charging–charging cycles and good rate performance of 152.7 mA h g^{-1} at 10 C in an organic electrolyte consisting of $LiPF_6$. The MOF-NC achieved the specific capacity of 269.9 F g^{-1} at a current density of 0.2 A g^{-1}. When the current density was increased to 6 A g^{-1}, it could still remain at 92.4% of the initial capacity after 2000 discharging–charging cycles. The Li-HSCs of WO_3/C//MOF-NC boast a large energy density of 159.97 W h kg^{-1} at a power density of 173.6 W kg^{-1}, which is larger for Li-HSCs than previously-reported Li-HSCs based on Nb_2O_5, MnO_2 and V_2O_5. The excellent properties of the Li-HSCs stem from the 3D hierarchical microspheres assembled by radically oriented WO_3/C nanorods and large-surface-area MOF-NC with a unique porous morphology and desired micro- and meso-porosities. The Li-HSC delivers an energy density much higher than commercial supercapacitors and it is comparable to that of commercial lithium-ion batteries with improved power densities, rendering promising applications in energy storage.

Fig. 7 Ragone plots comparing results of Li-HSCs. The Li-HSCs composed of WO_3/C//MOF-NC (black) are compared to Li-HSCs with Nb_2O_5/C//AC (red), V_2O_5-CNT//AC (blue), MOF-C//MOF-C symmetric supercapacitor (green), MOF-C//$Li_4Ti_5O_{12}$ hybrid system (magenta), HTO//AC (yellow) and MnO-GNS//HNC (wine).

Acknowledgements

Notes and references

1 F. Zhang, T. Zhang, X. Yang, L. Zhang, K. Leng, Y. Huang and Y. Chen, *Energy Environ. Sci.*, 2013, **6**, 1623.

2 A. D. Pasquier, I. Plitz, J. Gural, S. Menocal and G. Amatucci, *J. Power Sources*, 2003, **113**, 62.

3 V. Khomenko, E. Raymundo-Piñero and F. Béguin, *J. Power Sources*, 2008, **177**, 643.

4 M. Armand and J. M. Tarascon, *Nature*, 2008, **451**, 652.

5 M. S. Whittingham, *Chem. Rev.*, 2004, **104**, 4271.

6 P. Simon and Y. Gogotsi, *Nat. Mater.*, 2008, **7**, 845.

7 L. Ye, Q. Liang, Y. Lei, X. Yu, C. Han, W. Shen, Z. Huang, F. Kang and Q. Yang, *J. Power Sources*, 2015, **282**, 174.

8 H. S. Choi, J. H. Im, T. Kim, J. H. Park and C. R. Park, *J. Mater. Chem.*, 2012, **22**, 16986.

9 J. Wang, J. Liu, H. Yang, Z. Chen, J. Lin and Z. X. Shen, *J. Mater. Chem. A*, 2016, **4**, 7565.

10 S. Dsoke, B. Fuchs, E. Gucciardi and M. Wohlfahrt-Mehrens, *J. Power Sources*, 2015, **282**, 385.

11 S. Takai, M. Kamata, S. Fujine, K. Yoneda, K. Kanda and T. Esaka, *Solid State Ionics*, 1999, **123**, 165.

12 L. Tang, Y. Wang, Y. Li, H. Feng, J. Lu and J. Li, *Adv. Funct. Mater.*, 2009, **19**, 2782.

13 M. Sasidharan, N. Gunawardhana, M. Yoshio and K. Nakashima, *Mater. Res. Bull.*, 2012, **47**, 2161.

14 X. Wang, G. Li, Z. Chen, V. Augustyn, X. Ma, G. Wang, B. Dunn and Y. Lu, *Adv. Energy Mater.*, 2011, **1**, 1089.

15 H. Nakazawa, K. Sano, T. Abe, M. Baba and N. Kumagai, *J. Power Sources*, 2007, **174**, 838.

16 C. X. Guo, M. Wang, T. Chen, X. W. Lou and C. M. Li, *Adv. Energy Mater.*, 2011, **1**, 736.

17 A. L. M. Reddy, M. M. Shaijumon, S. R. Gowda and P. M. Ajayan, *Nano Lett.*, 2009, **9**, 1002.

18 L. Li, A. O. Raji and J. M. Tour, *Adv. Mater.*, 2013, **25**, 6298.

19 X. Duan, S. Xiao, L. Wang, H. Huang, Y. Liu, Q. Li and T. Wang, *Nanoscale*, 2015, **7**, 2230.

20 J. Lee, C. Jo, B. Park, W. Hwang, H. I. Lee and S. Yoon, *Nanoscale*, 2014, **6**, 10147.

21 S. Huang, Y. Cai, J. Jin, J. Liu, Y. Li, Y. Yu, H. Wang, L. Chen and B. Su, *Nano Energy*, 2015, **12**, 833.

22 A. Banerjee, K. K. Upadhyay, D. Puthusseri, V. Aravindan, S. Madhavi and S. Ogale, *Nanoscale*, 2014, **6**, 4387.

23 E. Lim, C. Jo, H. Kim, M. Kim, Y. Mun, J. Chun, Y. Ye, J. H. Wang, K. Ha, K. C. Roh, K. Kang, S. Yoon and J. Lee, *ACS Nano*, 2015, **9**, 7497–7505.

24 Z. Chen, V. Augustyn, J. Wen, Y. Zhang, M. Shen, B. Dunn and Y. Lu, *Adv. Mater.*, 2011, **23**, 791–795.

25 H. Colfen and M. Antonietti, *Angew. Chem., Int. Ed.*, 2005, **44**, 5576.

26 Y. Oaki and H. Imai, *Angew. Chem., Int. Ed.*, 2005, **44**, 6571.

27 M. Niederberger and H. Cölfen, *Phys. Chem. Chem. Phys.*, 2006, **8**, 3271.

28 S. A. Pervez, D. Kim, C. Doh, U. Farooq, H. Choi and J. Choi, *ACS Appl. Mater. Interfaces*, 2015, **7**, 7635–7643.

29 C. Lian, X. Xiao, Z. Chen, Y. Liu, E. Zhao, D. Wang and C. Chen, *Nano Res.*, 2016, **9**, 435.

30 R. Yi, F. Dai, M. L. Gordin, S. Chen and D. Wang, *Adv. Energy Mater.*, 2013, **3**, 295.

31 R. Yi, S. Chen, J. Song, M. L. Gordin, A. Manivannan and D. Wang, *Adv. Funct. Mater.*, 2014, **24**, 7433.

32 I. M. Szilágyi, B. Fórizs, O. Rosseler, Á. Szegedi, P. Németh, P. Király, G. Tárkányi, B. Vajna, K. Varga-Josepovits, K. László, A. L. Tóth, P. Baranyai and M. Leskelä, *J. Catal.*, 2012, **294**, 119.

33 T. Firkala, B. Fórizs, E. Drotár, A. Tompos, A. L. Tóth, K. Varga-Josepovits, K. László, M. Leskelä and I. M. Szilágyi, *Catal. Lett.*, 2014, **144**, 831.

34 R. Wu, J. Zhang, Y. Shi, D. Liu and B. Zhang, *J. Am. Chem. Soc.*, 2015, **137**, 6983–6986.

35 W. Li, F. Xia, J. Qu, P. Li, D. Chen, Z. Chen, Y. Yu, Y. Lu, R. A. Caruso and W. Song, *Nano Res.*, 2014, **7**, 903–916.

36 X. L. Hu, Q. M. Ji, J. P. Hill and K. Ariga, *CrystEngComm*, 2011, **13**, 2237.

37 F. Zheng, Y. Yang and Q. Chen, *Nat. Commun.*, 2014, **5**, 5261.

38 H. W. Wang, C. Guan, X. F. Wang and H. J. Fan, *Small*, 2015, **11**, 1470–1477.

39 V. Aravindan, N. Shubha, C. L. Chui and S. Madhavi, *J. Mater. Chem. A*, 2013, **1**, 6145.

40 L. F. Que, Z. B. Wang, F. D. Yu and D. M. Gu, *J. Mater. Chem. A*, 2016, **4**, 8716–8723.

41 M. Yang, Y. Zhong, J. Ren, X. Zhou, J. Wei and Z. Zhou, *Adv. Energy Mater.*, 2015, **5**, 1500550.